Engineering Fracture Mechanics 210 (2019) 189–202

Contents lists available at ScienceDirect

Engineering Fracture Mechanics

journal homepage: www.elsevier.com/locate/engfracmech

# Acoustic emission data analyses based on crumb rubber concrete beam bending tests

Qinghua Han[a], Guang Yang[a], Jie Xu[a,*], Zhengwu Fu[a], Giuseppe Lacidogna[b], Alberto Carpinteri[b]

[a] School of Civil Engineering, Tianjin University/Key Laboratory of Coast Civil Structure Safety of China Ministry of Education, Tianjin University, Tianjin 300072, China

[b] Department of Structural, Geotechnical and Building Construction, Politecnico di Torino, Turin 10129, Italy

ARTICLE INFO

*Keywords:*
Crumb rubber concrete
Acoustic emission
*b*-value method
Cluster analysis
RA value

ABSTRACT

Acoustic emission (AE) is a vital analysis method used to explain the fracture properties of concrete specimens. Four representative analyses methods, including the *b*-value method, AE signal intensity, average frequency (AF) versus RA (RA means rise time divided by the amplitude) value, and cluster analyses, are utilised to characterise and analyse the damage mechanisms and failure modes of three-point and four-point crumb rubber concrete bending beams with different rubber contents, including, 0%, 5%, 10%, and 15%. Tests and analysed results show that the fracture magnitude in the crumb rubber concrete is larger than that in the normal concrete before the main collapse stage. The improved *b*-value (*Ib*-value) fluctuations in local regions are more closely clustered with increase of rubber content. Based on intensity analyses, the severity ($S_r$) and historical index (*HI*) boundaries of the safe regions of crumb rubber concrete are proposed. Three clusters that correspond to the three different stages of the fracture process are mainly observed. There is a very clear distinction between the different clusters based on RA and AF values for all specimens. Furthermore, the AE rise time, ring down counts, energy, duration, and amplitude, are indicators used in the cracking mode characterization of the tested specimens.

## 1. Introduction

Acoustic emission (AE) is a non-destructive testing technique and a real-time monitoring method in engineering structures [1]. It has been used for damage detection and assessment. During the recent decades, the application of AE has received increased attention as a potential real time monitoring technique for concrete in engineering structures [2,3]. To assess the structural integrity of concrete structures, the AE signal analysis is useful to detect and monitor the micro-cracks and their growth during the entire fracture process in quasi-brittle materials [4–10]. AE signal analysis is conventionally used based on specific characteristics. The simplest analysis approach includes the AE counts, amplitude, energy, signal strength, rise time, hits, and frequency [11]. Several analyses methods based on AE signals, such as the *b*-value method, AE signal intensity, average frequency (AF) versus RA value (rise time divided by the amplitude), and cluster analyses, are utilised to analyse the damage mechanisms and failure modes of concrete structures.

Many scholars used the *b*-value analysis method to perform AE signal analyses [12–14]. The principle of this method is based on the fact that micro-cracks give rise to more AE events with smaller amplitude, while macro-cracks give rise to fewer AE events with

* Corresponding author.
*E-mail address:* jxu@tju.edu.cn (J. Xu).

https://doi.org/10.1016/j.engfracmech.2018.05.016
Received 27 February 2018; Received in revised form 9 May 2018; Accepted 10 May 2018
Available online 25 May 2018

larger amplitudes. Shiotani et al. [15,16] proposed the improved *b*-value (*Ib*-value) method using the statistical information of AE events. The *Ib*-value analysis has been determined to be feasible for monitoring slope failures, evaluation of rock fracture processes, and damage assessment of reinforced concrete (RC) beams [17]. The level of damage of a concrete structure can be characterised using intensity analysis (IA) of the AE signal. It can be used as an evaluation method to determine the integrity of the entire structure. The IA method has also formerly been applied by Nair for analysing RC members [18]. The IA plot is a plot of the historical index (*HI*) versus severity ($S_r$) and has exhibited a promising relationship and correlated well with the damage level of the specimens. The parameters *HI*, $S_r$, and the intensity analyses have been used by many scholars for concrete structures [19–21]. The fundamental of crack classification is the ability to classify tensile crack and shear crack in the structure. The parameters of utmost importance in the computation of the two indices are the AF and RA values [1]. Several researchers have adopted the values of AF and RA for crack classification on many types of materials and structures, such as for steel fibre reinforced concrete, cement based materials, and RC beams and bridges [7,22–27]. K-means clustering algorithm is an extensively used data clustering analysis method for AE signals [28,29]. Some studies show the identification methods of the clusters for AE signals from the tests of pre-stressed strands and Carbon Fiber Reinforced Polymer (CFRP)-specimens [30,31].

Crumb rubber concrete (CRC) is also known as recycled tire rubber-filled concrete and has been extensively studied during the last two decades [32,33]. Ever since the 1990's, different types of tests with different volumetric fractions had been conducted to investigate the static, dynamic, and fatigue mechanical behaviour of CRC by many scholars [34–43]. The first CRC pavement was built in 1999 by Professor Han Zhu [44]. Subsequently, CRC use had been extended to tennis courts, parking areas, bridge deck pavements, and in other applications [45,46]. In recent years, the CRC was employed in steel-concrete composite structures for the replacement of normal concrete [47–50]. Rubberised concrete has been studied using the AE technique for fatigue damage process [51] and fracture evaluation [52]. In spite of extensive work completed on the mechanical properties of CRC, the research aimed at the understanding of the fracture properties based on the crack mechanism. The study of micro-cracking and fracture properties in CRC is an important topic and its knowledge is needed to comment on the integrity of the structure. If the AE signal was detected and the connection between the AE signal and cracks was analysed, it can lead to many applications in practical engineering.

In this study, the crumb rubber concrete specimens with different rubber contents (0%, 5%, 10%, and 15%) are tested using three-point and four-point bending tests, and are monitored using the AE method. Some representative analyses methods, such as the *b*-value method, AE signal intensity, AF versus RA value, and cluster analyses, are utilised to characterise and analyse the damage mechanisms and failure modes of crumb rubber concrete.

## 2. Analysis methods

### 2.1. b-value method

The *b*-value analysis method was first used in seismic waves generated by earthquakes and the *b*-value has been recognised extensively by seismologists for quantifying seismicity [53–55]. The waves of AEs are similar to seismic waves, and the *b*-value method can also be applied to the AE field. The Gutenberg-Richter (GR) law [56] of seismicity can be modified for the AE analysis as follows [12–14]:

$$\log_{10}N = a - b\left(\frac{A_{\mathrm{dB}}}{20}\right) \tag{1}$$

where $N$ is the number of AE events with magnitudes greater than $A_{\mathrm{dB}}$, $A_{\mathrm{dB}}$ is the peak amplitude of the AE events in decibels, $a$ is the intercept along the $\log_{10}N$-axis, and $b$ is the slope of the regression line, also called the *b*-value of these AE events. From Eq. (1), a bigger *b*-value can be obtained when micro-cracks begin to form. In contrast, a smaller *b*-value can be obtained when macro-cracks develop. Shiotani et al. proposed the improved *b*-value (*Ib*-value) method after it had been applied successfully to geotechnical and concrete materials [15,57–59]. The *Ib*-value has been defined by utilising statistical values of AE events, and it can be calculated by

$$Ib = \frac{\log_{10}N(\mu - \alpha_1\sigma) - \log_{10}N(\mu + \alpha_2\sigma)}{(\alpha_1 + \alpha_2)\sigma} \tag{2}$$

where $\sigma$ and $\mu$ are the standard deviation and mean values of the amplitude distribution of the AE event group, respectively, and $\alpha_1$ and $\alpha_2$ are user-defined constants, which would represent the coefficients of the lower and upper limits of the amplitude. It is understood that the *Ib*-value is a transient feature that is updated with each new hit recorded during the fracture process. It should be sensitive enough to follow even small fracturing events, so the population $N$ is usually set to 100 recent hits [60].

### 2.2. AE signal intensity analysis

The damage of concrete structures can be characterised using the intensity analysis (IA) of the AE signal. Intensity analysis involves the plot of historical index (*HI*) and log severity ($\log_{10} S_r$), both of which are based on the AE signal strength [61]. AE signal strength takes the amplitude and duration into account, so it is the most effective parameter to determine the trend of the AE data [11].

The *HI* index measures changes in signal strength throughout the loading process. *HI*($t$) is calculated by using the following equation [62,63]:

**Table 1**
*K*-parameter for concrete structure.

| Number of hits, *N* | ≤50 | 51–200 | 201–500 | ≥501 |
|---|---|---|---|---|
| *K* | Not applicable | *N*-30 | 0.85*N* | *N*-75 |

$$HI(t) = \frac{N}{N-K}\frac{\sum_{i=K+1}^{N} S_{oi}}{\sum_{i=1}^{N} S_{oi}} \tag{3}$$

where $HI(t)$ is the historic index at time $t$, $N$ is the number of hits up to and including time $t$, $S_{oi}$ is the signal strength of the $i$th hit, and $K$ is an empirical parameter that depends upon the number of AE hits [1]. Table 1 shows the $K$-parameter for the concrete structure. $HI$ can be used to obtain the change curve of the cumulative signal strength versus time. This method can determine the onset of new damages for the specimen or structure.

The severity ($S_r$) is defined as the average signal strength for the $J$ hits that have the largest numerical value of signal strength. It can be calculated by [64] as

$$S_r = \frac{1}{J}\sum_{i=1}^{J} S_{oi} \tag{4}$$

where $S_r$ is the severity index, $S_{oi}$ is the $i$th-largest signal strength, and $J$ is an empirical constant related to the material for concrete structures (Table 2). Therefore, the $S_r$ refers to the average strength of the 50 signals with the largest peak amplitudes of signal strength.

### 2.3. Average frequency versus RA value analysis

According to RILEM, the average frequency (AF) is defined as the number of counts in a hit divided by the duration of the signal. The RA value is calculated from the rise time divided by the amplitude [65]. The AF is measured in kHz, while the value of RA is measured in μs/V. The two parameters can be calculated based on the following equations:

$$\text{RA} = \text{the rise time/ peak amplitude} \tag{5}$$

$$\text{AF} = \text{AE ringdown counts/ duration time} \tag{6}$$

Based on the relationship between the AF and RA value established by Ohtsu et al. [66], the cracks can be classified into tensile cracks and shear cracks (Fig. 1). A shear crack has occurred when the AE signal has high-RA and low-AF values. Meanwhile, tensile cracks have occurred when the AE signal has low-RA and high-AF values [11].

### 2.4. Cluster analysis

K-means clustering method aims at dividing the $n$-dimensional data set X into $k$-clusters by minimising a clustering criterion. However, the number of clusters $k$, is not known a priori. In this study, the Davies-Bouldin index, Dunn index, Rousseeuw's silhouette value, and Tou index, were calculated to test the reliability of the cluster results [67–70]. A flowchart diagram of the complete method is shown in Fig. 2.

#### 2.4.1. Cluster validation indices

(i) Davies-Bouldin index

The Davies-Bouldin (DB) index [67] is defined as follows:

$$\text{DB} = \frac{1}{M}\sum_{i=1}^{m} \max_{j=1,\cdots,M; j\neq i}(d_{ij}), \qquad \text{where} \quad d_{ij} = \frac{\sigma_i + \sigma_j}{d(c_i, c_j)} \tag{7}$$

where $M$ is the number of clusters, $\sigma_i$ is the average distance of all patterns in cluster $i$ to their cluster centres $c_i$ and $d(c_i, c_j)$ are the

**Table 2**
*J* value for concrete structures.

| Number of hits | < 50 | ≥50 |
|---|---|---|
| *J* value | Not applicable | 50 |

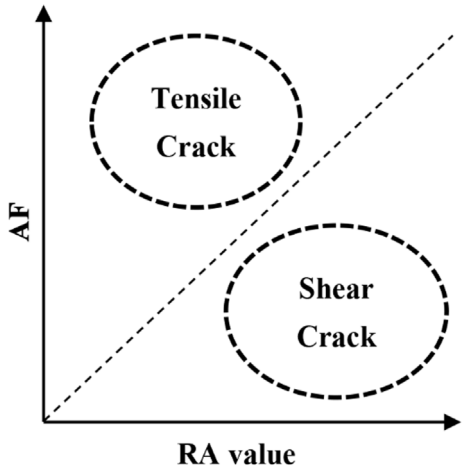


**Fig. 1.** Typical crack classification based on the relationship between the AF and RA values [66].

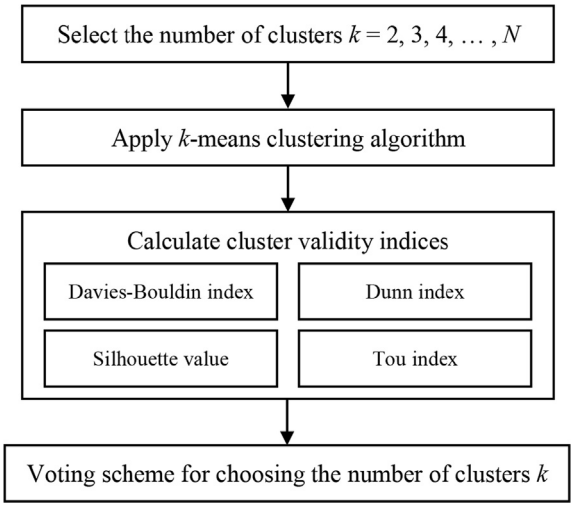


**Fig. 2.** Flowchart showing the cluster analysis process.

distances of the cluster centres $c_i$ and $c_j$. If the clusters $i$ and $j$ are compact, and theirs centres are far away from each other, then $d_{ij}$ is small. Thus, the DB index indicates good partitioning by value minimisation.

(ii) Dunn index

Dunn ($D$) index [68] is given by

$$D = \frac{d_{\min}}{d_{\max}} \tag{8}$$

where $d_{\min}$ is the smallest distance between two elements from different clusters, and $d_{\max}$ is the largest distance of two patterns from the same cluster. Clearly, the Dunn ($D$) index indicates good partitioning by value maximisation.

(iii) Rousseeuw's silhouette value

The silhouette ($s$) value [69] is defined as follows,

$$s(i) = \frac{b(i) - a(i)}{\max\{a(i), b(i)\}} \tag{9}$$

where $a(i)$ is the average distance of $i$ to all other patterns in cluster A, and $b(i)$ is the smallest average distance of $i$ to all the patterns in other clusters except cluster A. The silhouette ($s$) value indicates a good partitioning based on value maximisation.

(iv) Tou index

Tou (λ) index [70] is given by

$$\lambda(N_c) = \frac{\min D_{ij}}{\max D_j} \tag{10}$$

where $D_{ij}$ are the distances of each two cluster centres, and $D_j$ is the intra-set distance for each cluster. Optimal clusters occur when $\lambda(N_c)$ reaches a peak, and $N_c$ is optimal if $\lambda(N_c)$ is a global maximum.

#### 2.4.2. Voting scheme

Based on these four cluster validity measures, a voting scheme adapted from Günter and Bunke [71] was used to improve the automated determination of the optimal number of clusters. The voting scheme is described as follows: If the maximum number of clusters is $N$, the number of clusters with the best index performance is assigned to $(N-1)$ points. The number of clusters with the second-best performance is assigned to $(N-2)$ points. The number of clusters with the third-best performance is given $(N-3)$ points. Based on the same pattern, the clusters with the worst performance are each assigned to one point. Subsequently, the points of all four cluster validity indices are accumulated as a function of the number of clusters and are evaluated for their global maximum in points. The respective number of clusters is defined as numerically optimal and is thus selected for the current feature combination [31]. The strengths of different cluster validity indices are effectively combined by the voting scheme, while the weaknesses are reduced.

## 3. Description of bending tests

### 3.1. Raw materials and concrete mixture

The raw materials of CRC specimens used in the bending tests were derived from Ordinary Portland Cement, coarse aggregate (maximum size of 20 mm), sand, and rubber crumbs (1–2 mm). The mix proportions of crumb rubber concrete are shown in Table 3. The rubber content was divided into four groups, 0% (following the principle of the volume percentage method), 5%, 10%, and 15%, as in our previous research [47–50]. These four groups of concrete were designed to be of the same grade level, namely C30. The compressive strength of C30 is in the range of 35–45 MPa.

### 3.2. Specimen preparation

As shown in Fig. 3, the bending tests were carried out on a series of three-point bending specimens with different notch/depth ratios (0.15, 0.30, and 0.50) and a respective series of four-point bending specimens. Three specimens of each type (a total of 48 specimens: 36 specimens underwent three-point bending, and 12 specimens underwent four-point bending) were fabricated and tested for measuring the data during the fracture process. Geometric details of the specimens in the bending tests were listed in Table 4.

### 3.3. Testing arrangement

The electronic universal testing machines with capacities of 50 kN and 100 kN were used for three-point and four-point bending tests, respectively (see Fig. 4(a) and (c)). The Data Acquisition System for measuring dynamic and static strains (TST3827) was used for strain recording, and a PC based multi-channel monitoring system SAMOS AE$^{win}$ (Sensor based Acoustic Multi channel Operating System) that was manufactured by the Physical acoustic corporation (PAC) was used for AE recording. The main components of the AE system are eight AE sensors. The sensors used in the bending tests were R6α resonant type sensors. The sensors were coupled to the test specimen by means of the high vacuum grease couplant and were secured with tapes or special fixing devices (shown in Fig. 4(b) and (d)). All sensors were held firmly to the testing surface. The threshold for detecting AE was fixed at 40 dB to ensure a high signal-to-noise ratio. The three-point bending specimens were tested by controlling the mid-span downward displacement at the rate of 0.05 mm/min, and an electronic extensometer was used to measure the crack mouth opening displacement (CMOD). The four-point bending specimens were tested by force control at the rate of 0.167 kN/s.

**Table 3**
Mix Composition of CRC.

| Content of rubber particles | Rubber particles (kg/m$^3$) | Cement (kg/m$^3$) | Coarse aggregate (kg/m$^3$) | Sand (kg/m$^3$) | Water (kg/m$^3$) | Superplasticiser (kg/m$^3$) |
|---|---|---|---|---|---|---|
| 0% | 0 | 295 | 1087 | 839 | 165 | 2.174 |
| 5% | 50 | 400 | 703 | 1004 | 169 | 2.391 |
| 10% | 100 | 590 | 1230 | 412 | 168 | 6.522 |
| 15% | 150 | 590 | 1230 | 412 | 168 | 7.390 |

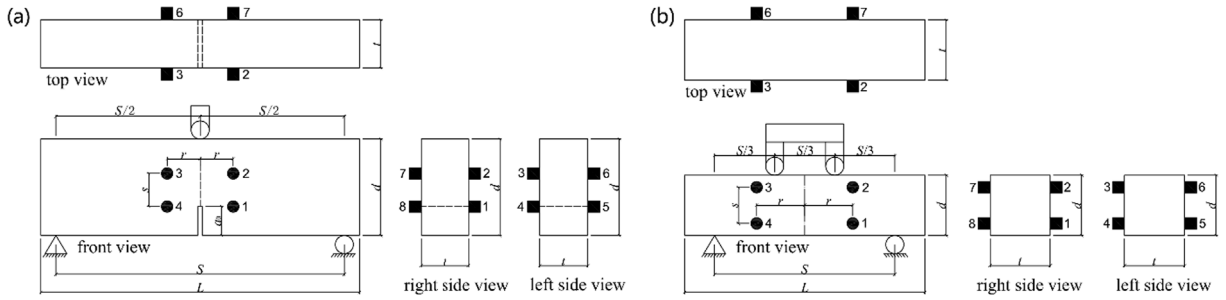


**Fig. 3.** Schematic diagrams of specimens: (a) three-point bending, and (b) four-point bending.

**Table 4**
Details of tested specimens.

| Type | No. | Notch details | | Dimensions of the specimen (mm) | | | | Sensors position (mm) | |
|---|---|---|---|---|---|---|---|---|---|
| | | Notch depth ($a_0$)(mm) | Notch/beam depth ratio ($a_0/d$) | Length ($L$) | Span ($S$) | Thickness ($t$) | Depth ($d$) | $r$ | $s$ |
| Three-point | A | 24 | 0.15 | 530 | 480 | 80 | 160 | 65 | 65 |
| Three-point | B | 48 | 0.30 | 530 | 480 | 80 | 160 | 55 | 55 |
| Three-point | C | 80 | 0.50 | 530 | 480 | 80 | 160 | 50 | 90 |
| Four-point | – | – | – | 400 | 300 | 100 | 100 | 80 | 60 |

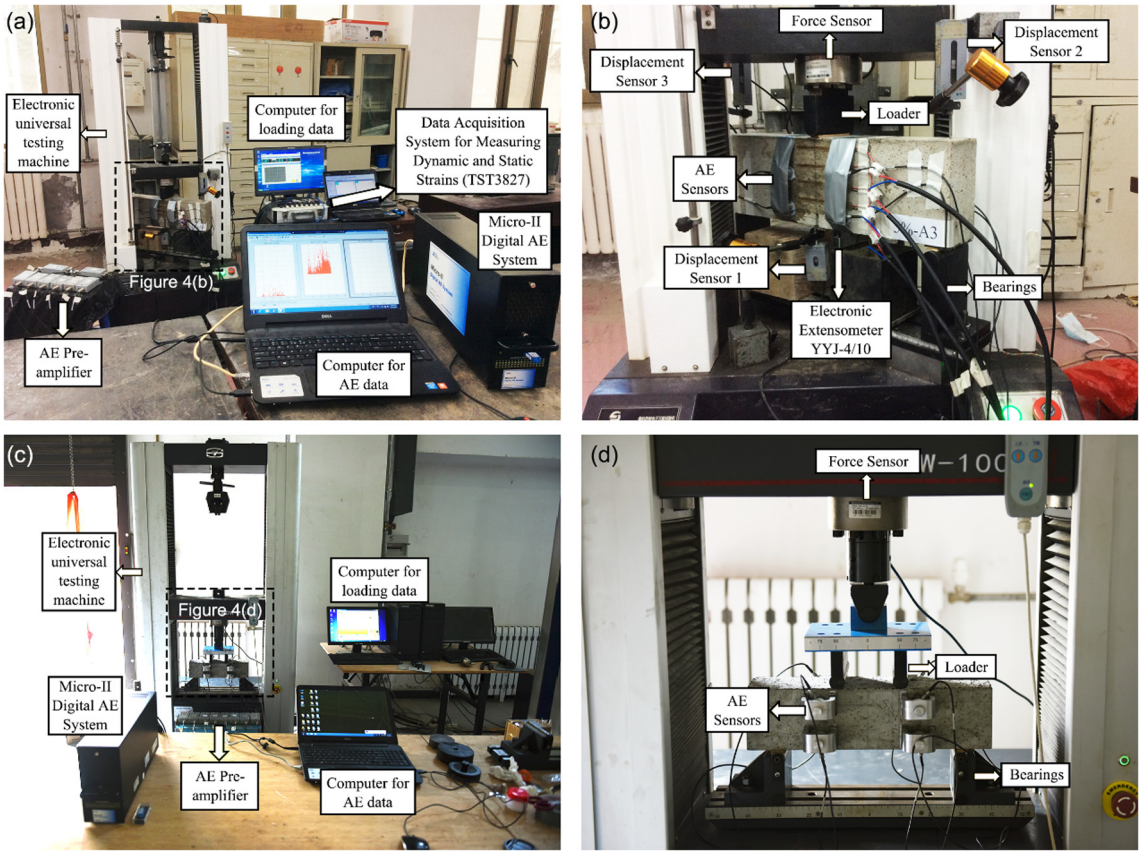


**Fig. 4.** (a, b) Overall views and details of used equipment for the three-point bending test setup, (c, d) Overall views and details of used equipment for the four-point bending test setup.

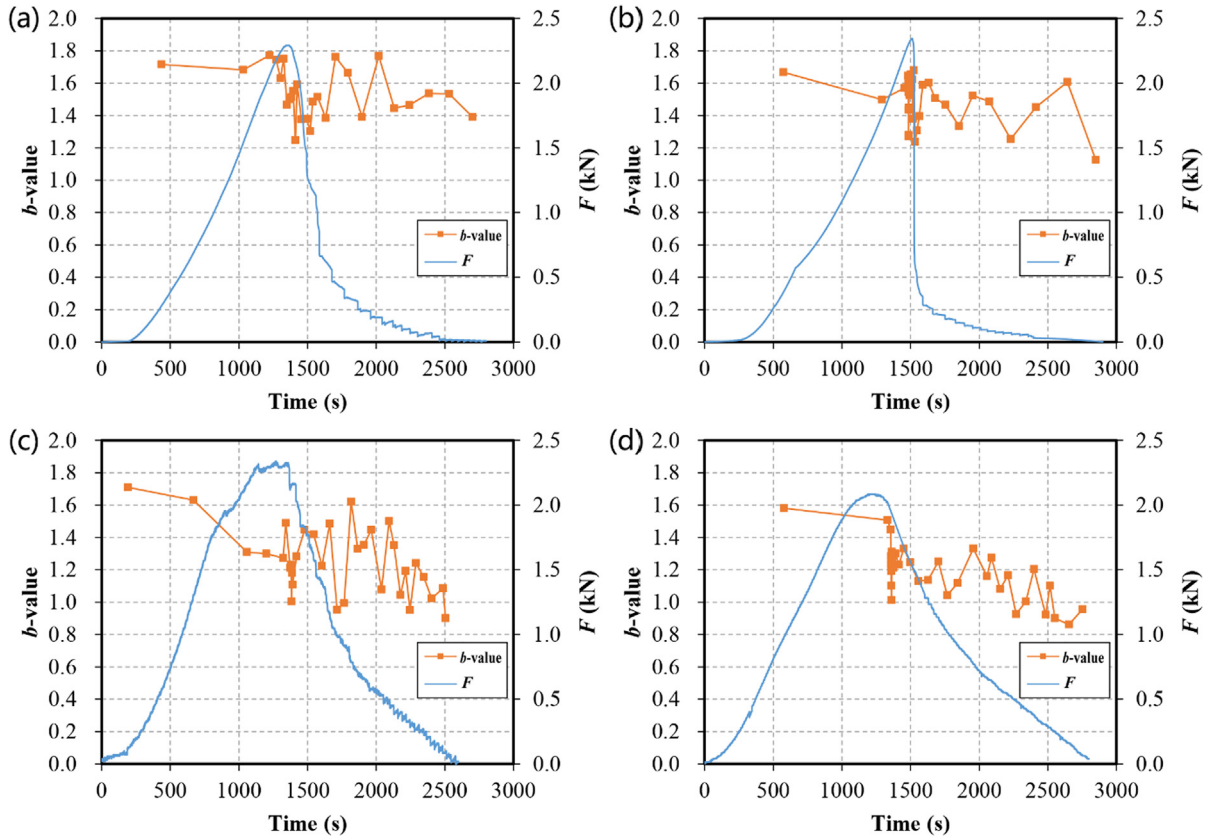


**Fig. 5.** Variations of *b*-value (orange points and curves) and load *F* (blue curves) versus time for specimens with different rubber contents (data from three-point bending test): (a) 0%, (b) 5%, (c) 10%, and (d) 15%. (For interpretation of the references to colour in this figure legend, the reader is referred to the web version of this article.)

## 4. Results and discussion

### *4.1. b-value analysis based on AE*

The *b*-value curves of the normal and crumb rubber concrete specimens are shown alongside the three-point bend loading curves in Fig. 5. At the early stages, the *b*-value curves show almost the same trend before the main cracks occurred. This stage refers to the formation of micro-cracks. From Fig. 5(a)–(d), there is an obvious decrease in the *b*-value curves around the location of the primary collapse stage (corresponding to the peak point of each loading curve), thereby revealing that the fracture patterns shifted from the micro-cracks to macro-cracks. We can see that the maximum, minimum, and difference of *b*-values for this stage decrease with the increase in the rubber contents (Table 5). This phenomenon can be explained as follows: the fracture magnitude in the crumb rubber concrete is larger than that in the normal concrete before the primary collapse stage, and the corresponding *b*-value is relatively smaller in the crumb rubber concrete. This means that the micro-cracks in the crumb rubber concrete are more in number than their number in the normal concrete. Furthermore, the fracture magnitude of the formation process for the main crack in crumb rubber concrete is smaller than normal concrete. Therefore, the *b*-value can reveal the difference in the fracture process between the normal concrete and the crumb rubber concrete at the primary collapse stage. It can also be found that the *b*-values for the final states decrease with the increase of the rubber contents. Thus, the fracture magnitudes increase as the rubber contents increase at the final stage.

The curves of the *Ib*-values of the concrete specimens with different rubber contents are shown together with four-point bending

**Table 5**
Maximum and minimum *b*-values for the main collapse stage.

| Rubber contents of concrete specimens | 0% | 5% | 10% | 15% |
|---|---|---|---|---|
| Maximum *b*-value for the main collapse stage | 1.773 | 1.679 | 1.488 | 1.418 |
| Minimum *b*-value for the main collapse stage | 1.248 | 1.218 | 1.049 | 1.012 |
| Maximum-Minimum | 0.525 | 0.461 | 0.439 | 0.406 |

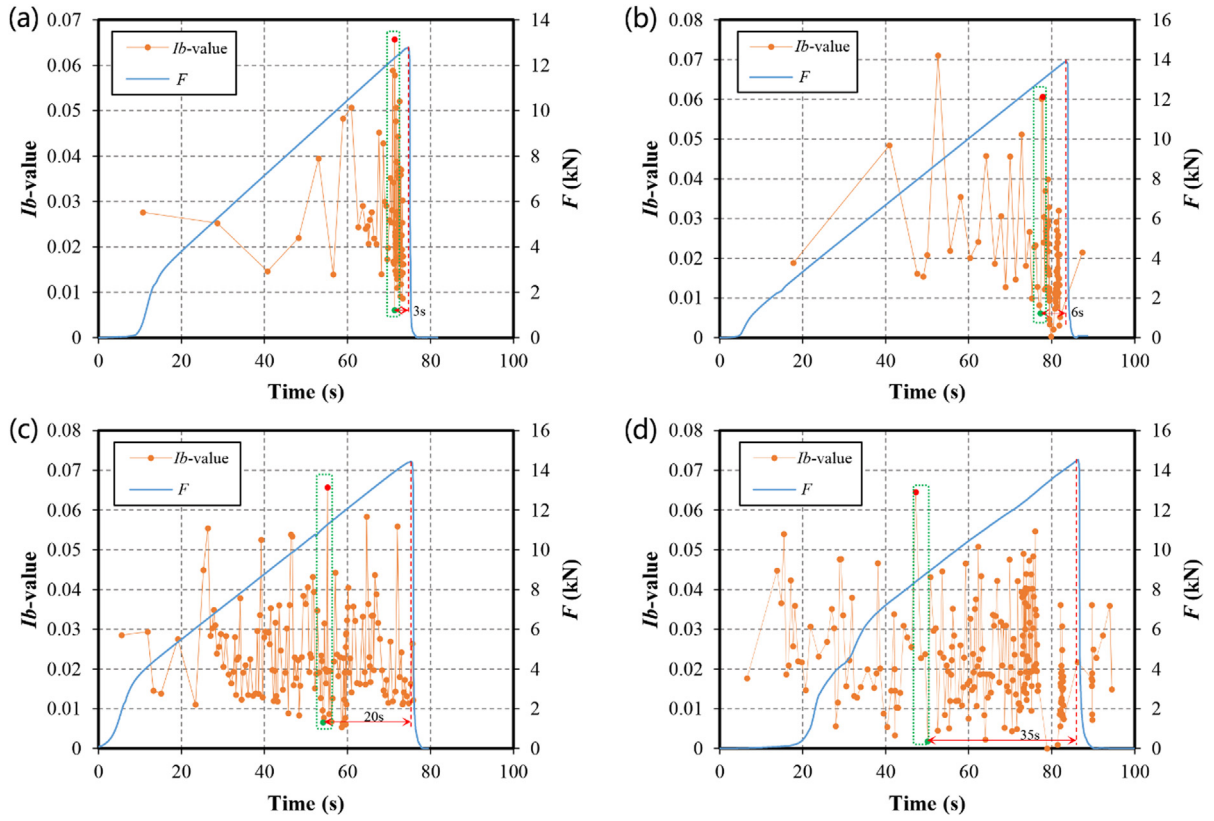


**Fig. 6.** *Ib*-value and load *F* versus time for specimens with different rubber contents (data were obtained from four-point bending tests): (a) 0%, (b) 5%, (c) 10%, and (d) 15%.

loading curves in Fig. 6. The *Ib*-value is calculated using 100 recent hits recorded during the fracture process. Based on Fig. 6(a)–(d), the *Ib*-value fluctuations during the loading process become more concentrated as the rubber contents increase. The instants of fractures of concrete specimens can be identified by the vertical drops of the loading curves. The fluctuations value (maximum minus minimum) are 0.058 (0%), 0.054 (5%), 0.059 (10%), and 0.062 (15%), as shown in the green dotted box of Fig. 6(a)–(d). In these four cases of CRC with different rubber contents, at the moment the *Ib*-value exhibits a strong fluctuation, the fracture moment drops and reaches a global minimum level with an end-value that is less than 0.01. Therefore, the degree of concentration for the fluctuations of the *Ib*-values can reveal the difference in the fracture process between the concrete specimens with different rubber contents. Furthermore, significant fluctuations in the *Ib*-values larger than 0.05 indicate an upcoming failure. This implies that approximately 3 s, 6 s, 20 s, and 35 s before the visible crack formation of the specimens with different rubber contents at 0%, 5%, 10%, and 15%, respectively. The strong fluctuation in the *Ib*-value is the precursor of the main collapse. The fluctuation 0.05 of the *Ib*-value can be considered as a threshold value to alert for the severity of the structural condition of the material. Furthermore, the time intervals between the onset of occurrence of the intense fluctuations (larger than 0.05) and the visible crack formation increase with the rubber contents, and thus concrete specimens with an increased rubber content provide longer warning time for us to deal with the fracture of the CRC specimens.

### *4.2. Intensity analysis (IA) based on AE signals*

The historical index (*HI*) and log severity ($\log_{10} S_r$) value of the specimens are shown in Fig. 7. The $\log_{10} S_r$ value is plotted on the left *y*-axis, while *HI* is plotted on the right *y*-axis. It can be observed that the four maximum values of the *HI*–time curves increase with increases in the rubber contents of the specimens (Fig. 7(a)), and these curves of crumb rubber concrete specimens have more than one peak during the fracture process. Conversely, the curve of the *HI*–time of normal concrete has only one peak at the moment of the main crack formation (at approximately 68 s). This phenomenon can also be observed in the $\log_{10} S_r$ –time curves, while each peak of *HI*–time curves corresponds to the abrupt increase of the $\log_{10} S_r$ –time curve. One of the peaks of the *HI*–time curve determines the onset of a newly formed primary specimen damage. Therefore, with the increase of the rubber contents of the concrete specimens, more macro-cracks with higher signal strength are created. The points with large $S_r$ and large *HI* values (the points in the upper right part of Fig. 7(c) with arrows) imply that the specimen is in a dangerous condition. It can be concluded that the proposed boundaries (the red rectangle box in Fig. 7(c)) of the safe regions of CRC are equal to $1 \times 10^6$ for $S_r$ and to 10 for *HI*. These two values are proposed for all specimens with or without rubber particles. However, *HI* values for the CRC specimens with more rubber contents are

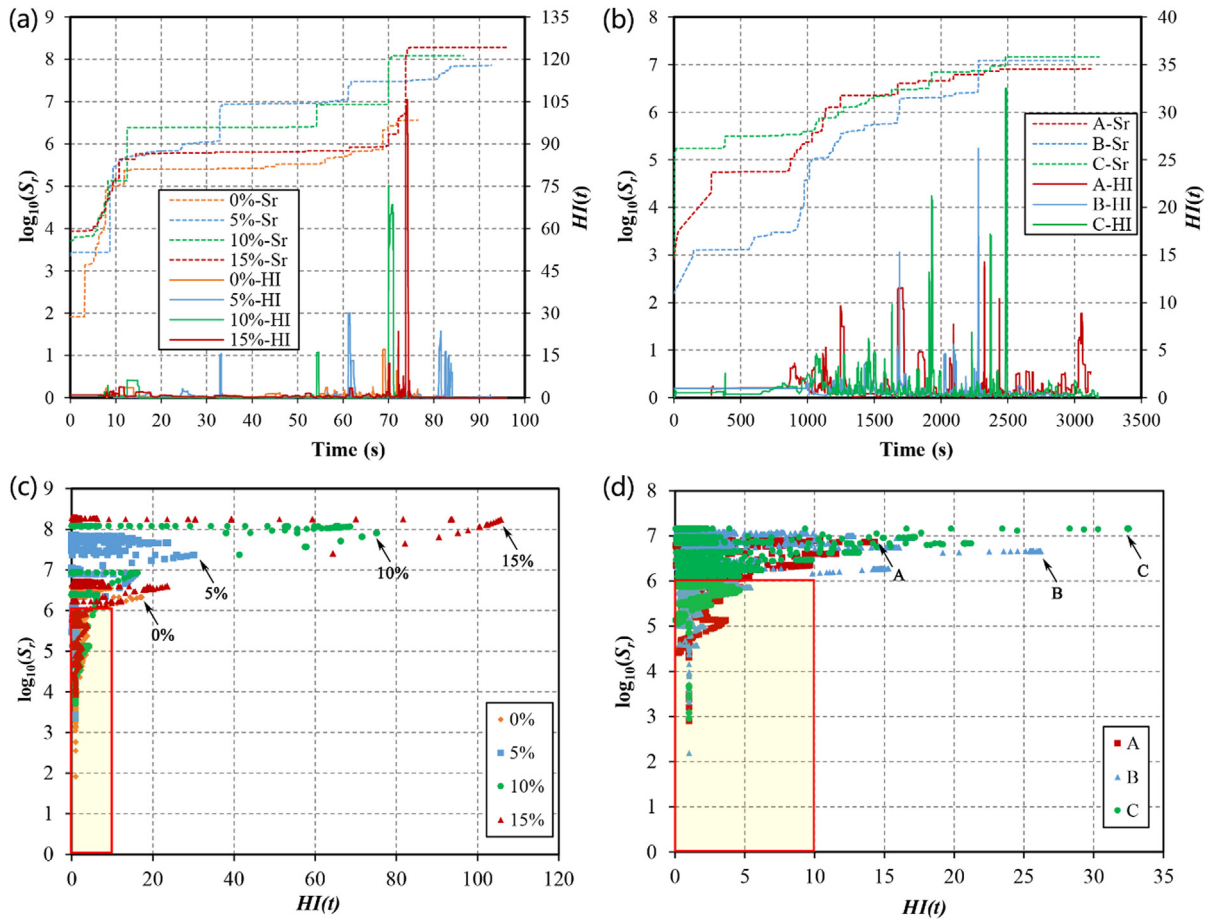


**Fig. 7.** *HI* and $\log_{10}(S_r)$ plots with (a) and (c) specimens of different rubber contents (data were obtained from four-point bending tests), (b, d) Corresponding plots for specimens with different notch depths (data were obtained from three-point bending tests).

1–2 times higher than the proposed value of 10. This means that increased rubber contents of CRC will provide more security reserve during the service.

Considering the specimens with different notch depths, the *HI* and $\log_{10} S_r$ values of the three-point bending specimens are shown in Fig. 7(b) and (d). It can be observed that the three maximum values of the *HI*–time curves increase with the notch depths and the slopes of the three $\log_{10} S_r$ –time curves become flatter with the increase of the notch depths. Furthermore, there are three, two, and one peak *HI* values that are almost or over the value of 15 for specimens A, B, and C, respectively. This means that the macro-cracks with large signal strength are created much easier for larger notch depths. It needs to be noted that for the concrete specimens or structures with defects in practical engineering, the same red-highlighted rectangular boxes with $S_r$ equal to $1 \times 10^6$ and *HI* equal to 10 can also be used, as shown in Fig. 7(c). We can also observe that these two values are also available, and the points in the red rectangular box ensure the safety of the specimens.

### 4.3. Cluster analysis of AE signals

Based on the AE signals of the three- and four-point bending tests, six AE parameters are used for cluster analyses. These included the rise time, counts, energy, duration, amplitude, and frequency centroids of gravity. Subsequently, the respective partitions for 2, 3, 4, 5, 6, and 7 clusters were calculated utilising the k-means algorithm. For each partition, the Davies-Bouldin index, Dunn index, Rousseeuw's silhouette value, and the Tou index were calculated. The voting scheme described in Section 2 can be used to evaluate the performance of each partition, and the voting points are shown in Table 6. The visualisation of this voting scheme is shown in Fig. 8, and the optimal number of the three clusters is detected using each of the cluster validity indices independently.

The quantity distribution of three clusters and cluster results for acoustic emission counts and frequency centroid of gravity are shown in Table 7 and Fig. 9. It can be observed that the quantity distribution of three clusters has obvious differences between normal concrete and crumb rubber concrete, that is, 81.567% for cluster 1 of normal concrete and over 99% for cluster 1 of crumb rubber concrete. As shown in Fig. 9, blue points (cluster 1) also have different value regions in reference to the frequency centroids of gravity and AE counts. The frequency centroids of gravity were within the ranges of 75–265 kHz and 25–215 kHz for normal concrete and

**Table 6**
Performance of cluster index values and corresponding voting values.

| Performance of cluster index values | Voting points |
|---|---|
| Best index performance | 6 |
| Second-best index performance | 5 |
| Third-best index performance | 4 |
| Fourth-best index performance | 3 |
| Fifth-best index performance | 2 |
| Worst performance | 1 |

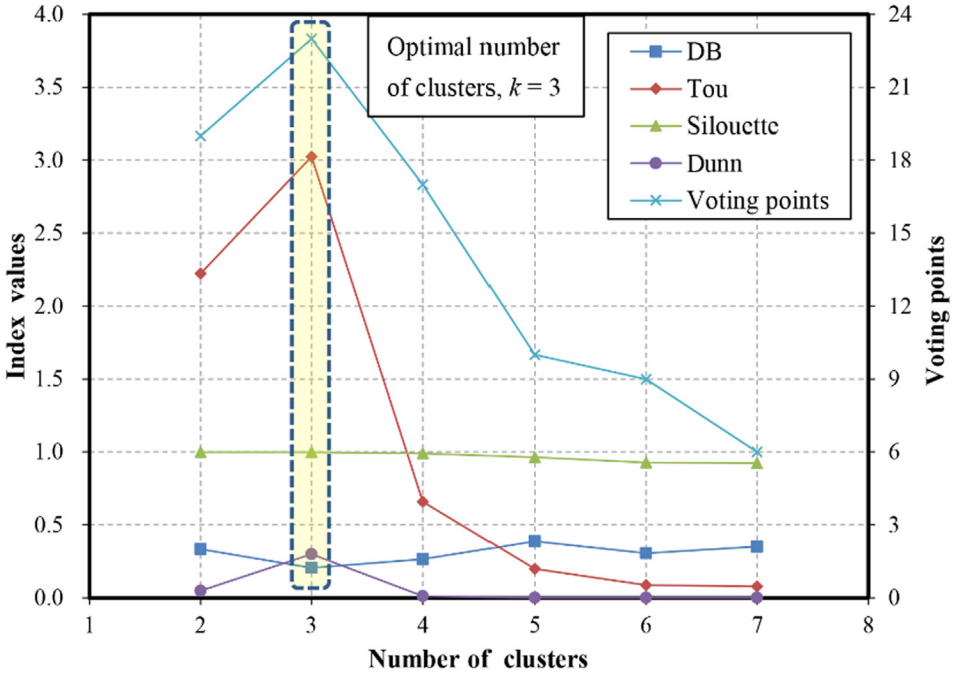


**Fig. 8.** Evaluation of several cluster index values in voting scheme.

**Table 7**
Quantity distribution of three clusters with specimens with different rubber contents.

| Rubber contents | 0% | 5% | 10% | 15% |
|---|---|---|---|---|
| Cluster 1 (%) (Blue points) | 81.567 | 99.662 | 99.499 | 99.831 |
| Cluster 2 (%) (Red points) | 16.258 | 0.142 | 0.183 | 0.055 |
| Cluster 3 (%) (Green points) | 2.175 | 0.196 | 0.318 | 0.114 |

crumb rubber concrete, respectively. Based on these two results, it can be concluded that micro-cracks in the crumb rubber concrete are more than those encountered in normal concrete. Furthermore, the signal frequency in the crumb rubber concrete is lower than that in the normal concrete. This means that increased rubber contents make the concrete specimens less brittle. The three clusters mainly correspond to three different stages for the fracture process: before fracture, after fracture and during fracture. The green points in Fig. 9(a)–(d) indicate the main collapse stage for the entire loading process. The most important feature of these points refers to the largest values of AE counts for each specimen, which refers to the AE signals of macro-cracks formation. We can conclude that when the main collapse begins, the values for the frequency centroid of gravity would be concentrated within the 50–100 kHz region for crumb rubber concrete. When cluster analysis is used for distinguishing the onset of the main collapse, this range (50–100 kHz) will constitute the criterion for the assessment of CRC.

### *4.4. Average frequency versus RA value analysis based on AE signals*

Owing to the large number of AE hits that occurred during the loading process, the crack mechanisms were analysed in terms of the temporal variation in the relative proportions. After the cracks were classified into two types (it is recommended to apply the RA/AF ratio of 50 [65], while ratio values for each hit that are smaller than 50 correspond to tensile cracks, or else the hit corresponds to

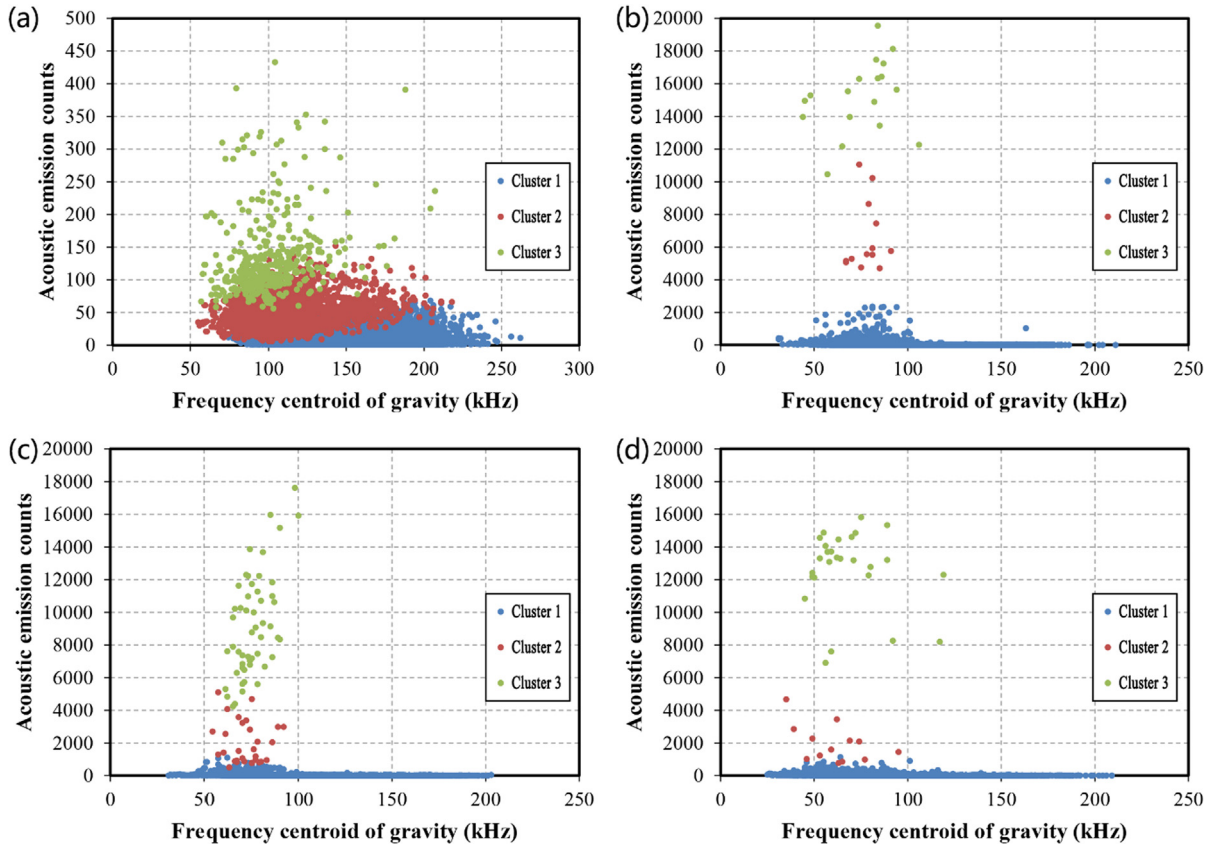


**Fig. 9.** Acoustic emission counts versus the frequency centroid of gravity with specimens with different rubber contents (data from four-point bending tests): (a) 0%, (b) 5%, (c) 10%, and (d) 15%.

shear cracks), a rolling average of the number of hits for each crack type was calculated for every hundred hits. The ratio of the number of tensile hits to the total number of hits corresponds to the left *y*-axis, while the ratio of the number of shear hits to the total number of hits corresponds to the right *y*-axis with inverted coordinates (Fig. 10). In order to facilitate the comparison of results from different specimens, the test time for each specimen is normalised to the total test time that equals 100. We can observe in Fig. 10(a) that almost 80% of the hits belong to the tensile type before fracture for CRC and normal concrete. When the normalised time is 70, each crumb rubber concrete curve exhibits a sudden drop to 20% of the tensile hits. Before this sudden drop, the curves of crumb rubber concrete specimens (especially for rubber contents of 10% and 15%) also exhibit downward trends to 50% of the tensile hits.

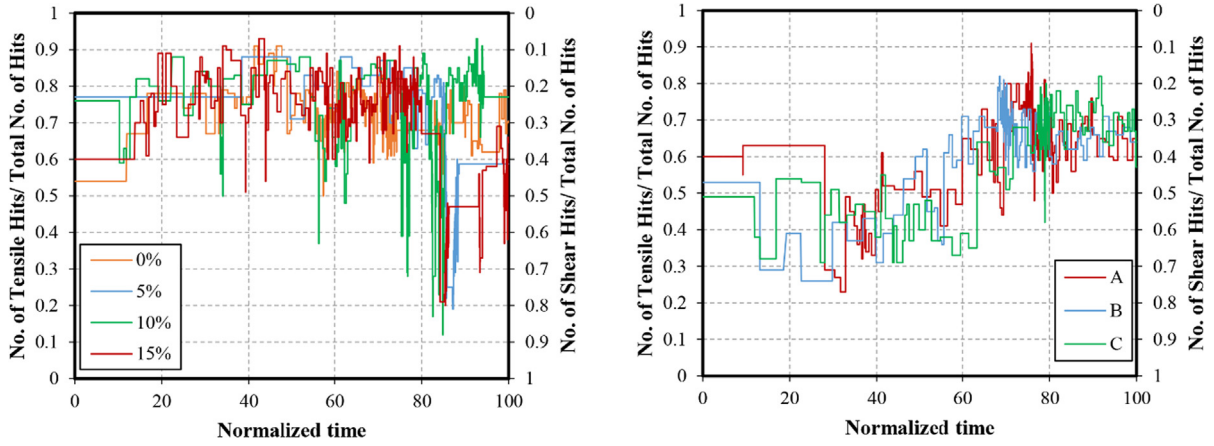


**Fig. 10.** Proportion of tensile and shear cracks to the total number of AE hits for specimens with (a) different rubber contents (data were obtained from four-point bending tests) and (b) different notch depths (data were obtained from three-point bending tests).

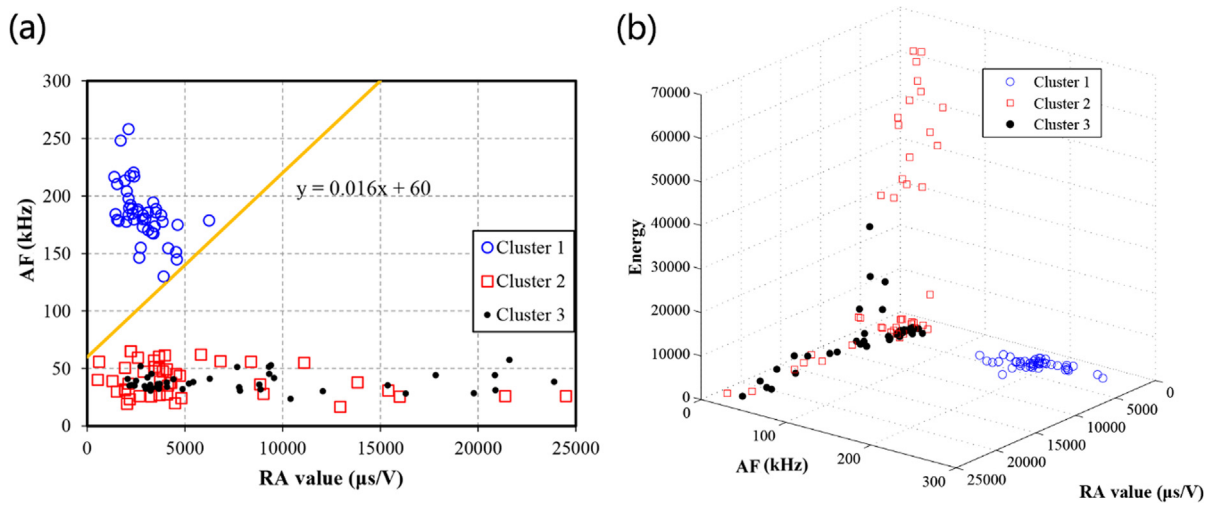


**Fig. 11.** (a) Correlation plot between AF and RA, and (b) three-dimensional correlation plot of the AE parameters for all three clusters for all three-point and four-point bending specimens.

However, the curve of the normal concrete specimen exhibits a minor decrease for tensile hits during and after fracture that is equal to 60%. This means that there is an obvious process that occurs and leads to the conversion of tensile cracks to shear cracks during the loading process for the crumb rubber concrete specimens. The results of the specimens for different notch depths are shown in Fig. 10(b). With the increase of notch depths, the gaps between the ratio of tensile hits before and after the fracture (before the fracture, the normalised time equals 60, and after it equals 70) increase by 0.12 (i.e. 0.62–0.50), 0.17 (i.e. 0.65–0.48), and 0.23 (i.e. 0.68–0.45). It can be concluded that larger notch depth specimens have smaller tensile cracks before and more shear cracks after the fracture.

Based on the test data obtained for cluster analysis, five parameters, namely rise time, AE counts, energy, duration, and amplitude were used in AF versus the RA value analysis. From Eqs. (5) and (6), the AF was calculated based on AE counts and duration, and the RA value was calculated based on rise time and amplitude. Thus, the AF and RA value can also be divided into three clusters using the same method presented in Section 4.3.

Fig. 11(a) shows the AF vs. RA value for the three clusters for all the 48 specimens (whereby 36 specimens underwent three-point bending, and 12 specimens underwent four-point bending tests). Each dot corresponds to the average of the entire population of hits for the specific cluster for each specimen (i.e. cluster 1, cluster 2, and cluster 3). There is a very clear discrimination between the different clusters based on these two AE parameters. Herein, we can obtain one straight line for the robust classification, as shown in Fig. 11(a). When the average frequency of the signal is higher than $0.016 \times RA + 60$, the crack can be classified into a tensile mode crack. This means that the cracks corresponding to the signals in cluster 1 are almost all tensile mode cracks. Furthermore, these signals in cluster 1 mainly occur before the formation of the main crack. It can be concluded that the tensile cracks mostly occur before the fracture. The cracks corresponding to the signals in clusters 2 and 3 are almost all shear mode cracks. Another parameter showing high sensitivity to the cluster pattern is energy. This can be observed in Fig. 11(b), where the entire population comprising almost 150 points is included in the three-dimensional space for all three clusters. We can see that the points (red hollow blocks) of cluster 2 have higher energies than those of the points of the other two clusters. Thus, these points correspond to the formation of the main fracture stage. It can also be observed that the black points of cluster 3 have lower energies, and average frequencies in the range of 25–50 kHz. Furthermore, the blue hollow points of cluster 1 are classified obviously for the lowest energy, small RA value, and highest average frequency in the range of 120–260 kHz. The results listed above reveal that the fracture process enables the characterisation of the different clusters reliably using AF, RA, and energy monitored non-destructively. The fact that the different populations of signals are totally separated into three different clusters shows that these five AE parameters (rise time, counts, energy, duration, amplitude) are really strong indicators to be used in cracking mode characterisation for crumb rubber concrete specimens.

## 5. Conclusions

In this study, four analyses methods are used to deal with the AE data of three-point and four-point bending tests of crumb rubber concrete and normal concrete specimens. The conclusions are summarised as follows:

(1) The *b*-value analysis method was used to study the fracture magnitude of concrete specimens. The fracture magnitude in the crumb rubber concrete was larger than that in the normal concrete before the main collapse stage, and the corresponding *b*-value was relatively smaller in the crumb rubber concrete. The fracture magnitudes for the final stage increased as a function of the rubber content since the *b*-values decreased.
(2) The trend of the *Ib*-value can reflect the development of cracks in the specimens. Furthermore, the fluctuation of the *Ib*-values in

local regions were more concentrated with the increase of rubber contents. Fluctuations for *Ib*-value of the order of 0.05 can be considered as the threshold to alert attention to the severity of the CRC and normal concrete specimens. Increased rubber contents of concrete specimens provide longer warning times for us to deal with the fracture of CRC specimens.

(3) Intensity analyses were based on the plot of historical index (*HI*) and severity ($\log_{10} S_r$). Based on the peaks and abrupt increase of these two indices, it can be concluded that more macro-cracks with higher signal strengths were created with the increase of the rubber content of the specimens. The maximum values of *HI* with concurrently high $S_r$ values are the unsafe points. The proposed boundaries for the safe region of CRC were equal to $1 \times 10^6$ for the $S_r$ and 10 for *HI*. *HI* values for the CRC specimens with increased rubber contents were 1–2 times the proposed value of 10. Thus, increased rubber content of CRC will provide more security reserve.

(4) Six AE parameters were used for cluster analysis. The respective partitions for clusters were calculated utilising the k-means algorithm. Four indices were utilised for the voting scheme to deal with the optimum number of the three clusters. The three clusters mainly corresponded to three different stages for the fracture process: before, after, and during fractures. When the main collapse occurred, the values for the frequency centroid of gravity would be concentrated in the frequency range of 50–100 kHz for CRC.

(5) The cracking failure modes of the crumb rubber concrete were analysed based on the RA and AF values. As the load increased, the type of cracks transformed from tensile cracks to shear cracks. Furthermore, larger notch depth specimens had fewer tensile cracks before and more shear cracks after the fracture.

(6) For all specimens in the three-point and four-point bending tests, there was a very clear discrimination between the different clusters based on the RA and AF values. Furthermore, the fracture process can be characterised by the different clusters reliably using AF, RA, and energy, which are monitored non-destructively. Therefore, the AE rise time, ring-down counts, energy, duration, and amplitude, are strong indicators used for CRC and normal concrete specimens in cracking mode characterisation.

## Acknowledgements

The authors would like to thank the National Natural Science Foundation of China (No. 51525803 & No. 51408408 & No. 51708403), Tianjin Natural Science Foundation (16JCQNJC07400) and Science and technology project of MOHURD (2016K3004) for providing the fund to carry out this research works.

## Appendix A. Supplementary material

Supplementary data associated with this article can be found, in the online version, at http://dx.doi.org/10.1016/j.engfracmech.2018.05.016.

## References

[1] Li D, Chen Z, Feng Q, Wang Y. Damage analysis of CFRP-confined circular concrete-filled steel tubular columns by acoustic emission techniques. Smart Mater Struct 2015;24(8):085017.
[2] Nielsen J, Griffin DF. Acoustic emission of plain concrete. J Test Eval 1977;5(6):476–83.
[3] Ohtsu M, Shigeishi M, Iwase H, Koyanagi W. Determination of crack location, type and orientation in concrete structures by acoustic emission. Mag Concrete Res 1991;43(155):127–34.
[4] Park HS, Lee HM, Adeli H, Lee I. A new approach for health monitoring of structures: terrestrial laser scanning. Comput-Aided Civ Inf 2007;22(1):19–30.
[5] Huang RY, Mao IS, Lee HK. Exploring the deterioration factors of RC bridge decks: a rough set approach. Comput-Aided Civ Inf 2010;25(7):517–29.
[6] Li H, Huang Y, Chen WL, Ma ML, Tao DW. Estimation and warning of fatigue damage of FRP stay cables based on acoustic emission techniques and fractal theory. Comput-Aided Civ Inf 2011;26(7):500–12.
[7] Aggelis DG. Classification of cracking mode in concrete by acoustic emission parameters. Mech Res Commun 2011;38(3):153–7.
[8] Carpinteri A, Xu J, Lacidogna G, Manuello A. Reliable onset time determination and source location of acoustic emissions in concrete structures. Cement Concrete Comp 2012;34(4):529–37.
[9] Mpalaskas AC, Thanasia OV, Matikas TE, Aggelis DG. Mechanical and fracture behavior of cement-based materials characterized by combined elastic wave approaches. Constr Build Mater 2014;50:649–56.
[10] Han Q, Xu J, Carpinteri A, Lacidogna G. Localization of acoustic emission sources in structural health monitoring of masonry bridge. Struct Control Hlth 2015;22(2):314–29.
[11] Noorsuhada MN. An overview on fatigue damage assessment of reinforced concrete structures with the aid of acoustic emission technique. Constr Build Mater 2016;112:424–39.
[12] Colombo IS, Main IG, Forde MC. Assessing damage of reinforced concrete beam using “b-value” analysis of acoustic emission signals. J Mater Civil Eng 2003;15(3):280–6.
[13] Carpinteri A, Lacidogna G, Manuello A. The b-value analysis for the stability investigation of the ancient Athena Temple in Syracuse. Strain 2011;47:e243–53.
[14] Carpinteri A, Lacidogna G, Puzzi S. From critical to final collapse: Evolution of the b-value from 1.5 to 1.0. Chaos Soliton Fract 2009:843–53.
[15] Shiotani T, Fujii K, Aoki T, Amou K. Evaluation of progressive failure using AE sources and improved b-value on slope model tests. Prg Acoust Emission VII JSNDI 1994;7:529–34.
[16] Shiotani T, Ohtsu M, Ikeda K. Detection and evaluation of AE waves due to rock deformation. Constr Build Mater 2001;15(5–6):235–46.
[17] Yun HD, Choi WC, Seo SY. Acoustic emission activities and damage evaluation of reinforced concrete beams strengthened with CFRP sheets. NDT & E Int 2010;43(7):615–28.
[18] Nair A. Acoustic Emission Monitoring and Quantitative Evaluation of Damage in Reinforced Concrete Members and Bridges (Master of Science in Civil Engineering), Kerala University; 2006.
[19] Degala S, Rizzo P, Ramanathan K, Harries KA. Acoustic emission monitoring of CFRP reinforced concrete slabs. Constr Build Mater 2009;23(5):2016–26.
[20] Lovejoy SC. Development of Acoustic Emissions Testing Procedures Applicable to Conventionally Reinforced Concrete Deck Girder Bridges Subjected to Diagonal Tension Cracking (Ph.D. thesis), Oregon State University; 2006.
[21] Golaski L, Gebski P, Ono K. Diagnostics of reinforced concrete bridges by acoustic emission. J Acoust Emission 2002;20:83–98.

[22] Aggelis DG, Mpalaskas AC, Ntalakas D, Matikas TE. Effect of wave distortion on acoustic emission characterization of cementitious materials. Constr Build Mater 2012;35:183–90.
[23] Aggelis DG, Soulioti DV, Barkoula NM, Paipetis AS, Matikas TE. Influence of fiber chemical coating on the acoustic emission behavior of steel fiber reinforced concrete. Cement Concrete Comp 2012;34(1):62–7.
[24] Aggelis DG, Mpalaskas AC, Matikas TE. Investigation of different fracture modes in cement-based materials by acoustic emission. Cement Concrete Res 2013;48:1–8.
[25] Ohno K, Ohtsu M. Crack classification in concrete based on acoustic emission. Constr Build Mater 2010;24(12):2339–46.
[26] Shiotani T. Recent advances of AE technology for damage assessment of infrastructures. J Acoust Emission 2012;30:76–99.
[27] Shahidan S, Pulin R, Bunnori NM, Holford KM. Damage classification in reinforced concrete beam by acoustic emission signal analysis. Constr Build Mater 2013;45:78–86.
[28] Godin N, Huguet S, Gaertner R. Integration of the Kohonen's self-organising map and k-means algorithm for the segmentation of the AE data collected during tensile tests on cross-ply composites. NDT&E Int 2005;38(4):299–309.
[29] Godin N, Huguet S, Gaertner R, Salmon L. Clustering of acoustic emission signals collected during tensile tests on unidirectional glass/polyester composite using supervised and unsupervised classifiers. NDT&E Int 2004;37(4):253–64.
[30] Ercolino M, Farhidzadeh A, Salamone S, Magliulo G. Detection of onset of failure in prestressed strands by cluster analysis of acoustic emissions. Struct Monit Maint 2015;2(4):339–55.
[31] Sause MGR, Gribov A, Unwin AR, Horn S. Pattern recognition approach to identify natural clusters of acoustic emission signals. Pattern Recogn Lett 2012;33(1):17–23.
[32] Eldin NN, Senouci AB. Rubber-tired particles as concrete aggregate. J Mater Civil Eng 1994;5(4):478–96.
[33] Siddique R, Naik TR. Properties of concrete containing scrap-tire rubber–an overview. Waste Manage 2004;24(6):563–9.
[34] Eldin NN, Senouci AB. Measurement and prediction of the strength of rubberized concrete. Cement Concrete Comp 1994;16(4):287–98.
[35] Toutanji HA. The use of rubber tire particles in concrete to replace mineral aggregates. Cement Concrete Comp 1996;18(2):135–9.
[36] Fedroff D, Ahmad S, Savas B. Mechanical properties of concrete with ground waste tire rubber. Transport Res Rec: J Transport Res Board 1996;1532(1):66–72.
[37] Li G, Garrick G, Eggers J, Abadie C, Stubblefield MA, Pang SS. Waste tire fiber modified concrete. Compos Part B-Eng 2004;35(4):305–12.
[38] Khaloo AR, Dehestani M, Rahmatabadi P. Mechanical properties of concrete containing a high volume of tire-rubber particles. Waste Manage 2008;28(12):2472–82.
[39] Zheng L, Huo XS, Yuan Y. Experimental investigation on dynamic properties of rubberized concrete. Constr Build Mater 2008;22(5):939–47.
[40] Najim KB. Mechanical and dynamic properties of self-compacting crumb rubber modified concrete. Constr Build Mater 2012;27(1):521–30.
[41] Youssf O, Elgawady MA, Mills JE. Experimental investigation of crumb rubber concrete columns under seismic loading. Structures 2015;3:13–27.
[42] Topçu BI. The properties of rubberized concrete. Cement Concrete Res 1995;25:304–10.
[43] Hernández-Olivares F, Barluenga G. Fire performance of recycled rubber-filled high-strength concrete. Cement Concrete Res 2004;34(1):109–17.
[44] Zhu H. Rubber crumbs in concrete. Concrete Technology Today 2003;135(8):30–3.
[45] Hernández-Olivares F, Barluenga G, Bollati M, Witoszek B. Static and dynamic behaviour of recycled tyre rubber-filled concrete. Cement Concrete Res 2002;32(10):1587–96.
[46] Eldin NN, Senouci AB. Rubber-tire particles as concrete aggregate. J Mater Civil Eng 1993;5(4):478–96.
[47] Han Q, Wang Y, Xu J, Xing Y. Static behavior of stud shear connectors in elastic concrete-steel composite beams. J Constr Steel Res 2015;113:115–26.
[48] Han Q, Wang Y, Xu J, Xing Y. Fatigue behavior of stud shear connectors in steel and recycled tyre rubber-filled concrete composite beams. Steel Compos Struct 2016;22(2):353–68.
[49] Han Q, Wang Y, Xu J, Xing Y, Yang G. Numerical analysis on shear stud in push-out test with crumb rubber concrete. J Constr Steel Res 2017;130:148–58.
[50] Han Q, Yang G, Xu J, Wang Y. Fatigue analysis of crumble rubber concrete-steel composite beams based on XFEM. Steel Compos Struct 2017;25(1):57–65.
[51] Wang C, Zhang Y, Ma A. Investigation into the fatigue damage process of rubberized concrete and plain concrete by AE analysis. J Mater Civil Eng 2011;23(7):953–60.
[52] Xu J, Fu Z, Han Q, Lacidogna G, Carpinteri A. Micro-cracking monitoring and fracture evaluation for crumb rubber concrete based on acoustic emission techniques. Struct Health Monit 2017;7:1–13.
[53] Han Q, Carpinteri A, Lacidogna G, Xu J. Fractal analysis and yule statistics for seismic prediction based on 2009 L'Aquila earthquake in Italy. Arab J Geosci 2015;8(5):2457–65.
[54] Smith WD. The b-value as an earthquake precursor. Nature 1981;289(5794):136–9.
[55] Han Q, Wang L, Xu J, Carpinteri A, Lacidogna G. A robust method to estimate the b-value of the magnitude-frequency distribution of earthquakes. Chaos Soliton Fract 2015;81(A):103–10.
[56] Gutenberg B, Richter CF. Frequency of earthquakes in California. B Seismol Soc Am 1994;34(4):185–8.
[57] Shiotani T, Ohtsu M. Prediction of slope failure based on AE activity. In ASTM Special Technical Publication, (West Conshohocken, PA: ASTM International), 1999:156–72.
[58] Shiotani T, Ohtsu M, Monma K. Rock failure evaluation by AE improved b-value. The Second Japan-US Symposium on Advances in NDT Proceedings Book, JSNDI, 1999:421–6.
[59] Shiotani T, Yuyama S, Li ZW, Ohtsu M. Application of AE improved b-value to quantitative evaluation of fracture process in concrete materials. J Acous Emission 2001;19:118–33.
[60] Aggelis DG, Soulioti DV, Sapouridis N, Barkoula NM. Paipetis AS, Matikas TE. Acoustic emission characterization of steel fibre reinforced concrete during bending. Proceedings of SPIE-The International Society for Optical Engineering 2010;7649:764912.
[61] Chotickai P. Acoustic Emission Monitoring of Prestressed Bridge Girders with Premature Concrete Deterioration (Master of Science in Engineering), The University of Texas; 2001.
[62] Benedetti MD, Nanni A (2014). Acoustic emission intensity analysis for in situ evaluation of reinforced concrete slabs. J Mater Civil Eng 2014;26(1):6–13.
[63] Li D, Cao H, Ou J. Fracture behavior and damage evaluation of polyvinyl alcohol fiber concrete using acoustic emission technique. Mater Design 2012;40:205–11.
[64] Fowler TJ, Blessing JA, Conlisk PJ, Swanson TL. The MONPAC system. J Acoust Emission 1989;8(3):1–8.
[65] RILEM Technical Committee. (Ohtsu M). Recommendation of RILEM TC 212-ACD: acoustic emission and related NDE techniques for crack detection and damage evaluation in concrete. Mater Struct 2010;43:1187–9.
[66] Ohtsu M, Isoda T, Tomoda Y. Acoustic emission techniques standardized for concrete structures. J Acoust Emission 2007;25:21–32.
[67] Davies DL, Bouldin DW. A cluster separation measure. IEEE T Pattern Anal 1979;1(2):224.
[68] Dunn J. Well separated clusters and optimal fuzzy partitions. Journal of Cybernetics 1974;4(1):95–104.
[69] Rousseeuw PJ. Silhouettes: a graphical aid to the interpretation and validation of cluster analysis. J Comput Appl Math 1987;20:53–65.
[70] Tou JT. DYNOC-a dynamic optimal cluster-seeking technique. Int J Comput Inf Sci 1979;8(6):541–7.
[71] Günter S, Bunke H. Validation indices for graph clustering. Pattern Recogn Lett 2003;24(8):1107–13.